

Surface-State-Driven Anomalous Hall Effect in Altermagnetic MnTe Films

Ling-Jie Zhou^{1,8}, Zi-Jie Yan^{1,8}, Hongtao Rong^{1,8}, Yufei Zhao^{1,2,8}, Pu Xiao¹, Lok-Kan Lai¹,
Zhiyuan Xi¹, Ke Wang³, Tibendra Adhikari⁴, Ganesh P. Tiwari⁴, Zhong Lin^{4,5}, Pascal Manuel⁶,
Fabio Orlandi⁶, Dmitry Khalyavin⁶, Alexander J. Grutter⁷, Chao-Xing Liu¹, Binghai Yan^{1,2}, and
Cui-Zu Chang¹

¹ Department of Physics, The Pennsylvania State University, University Park, PA 16802, USA

² Department of Condensed Matter Physics, Weizmann Institute of Science, Rehovot 7610001, Israel

³ Materials Research Institute, The Pennsylvania State University, University Park, PA 16802, USA

⁴ Department of Physics, Applied Physics and Astronomy, Binghamton University, Binghamton, NY 13902, USA

⁵ Materials Science and Engineering Program, Binghamton University, Binghamton, NY 13902, USA

⁶ ISIS Neutron and Muon Source, STFC Rutherford Appleton Laboratory, Harwell Campus OX11 0QX, Oxfordshire, UK

⁷ Center for Neutron Research, National Institute of Standards and Technology, Gaithersburg, MD 20899, USA

⁸ These authors contributed equally: Ling-Jie Zhou, Zi-Jie Yan, Hongtao Rong, and Yufei Zhao
Corresponding authors: binghai.yan@psu.edu (B. Y.); cxc955@psu.edu (C.-Z. C.)

Abstract: Altermagnets have recently emerged as a new class of magnetic materials that combine compensated magnetic order with spin-split electronic band structures. In this work, we employ molecular beam epitaxy to grow MnTe thin films with controlled thickness on InP(111)A substrates. By performing angle-resolved photoemission spectroscopy

measurements, we observe a large spin splitting of \sim 230 meV for bulk bands well below the Fermi level and identify surface states that cross the Fermi level. Electrical transport measurements reveal that a robust anomalous Hall (AH) effect persists down to 2 K and an AH sign reversal occurs near 175 K. By systematically tuning film thickness, growth conditions, and interfacial structure, we demonstrate that the AH response in MnTe films originates from the Berry curvature of surface states rather than from bulk bands. Our first-principles calculations reveal that this surface-state-driven AH effect is imprinted by the bulk altermagnetic order and remains unchanged for terminations with opposite Mn magnetic orientations. Our results establish a unique surface transport probe of bulk altermagnetism, demonstrate interface engineering as an effective route to generate and control the AH effect in altermagnets, and provide a unified understanding of the AH response in altermagnetic MnTe films.

Main text: Magnetic materials have traditionally been classified into two categories: ferromagnets and antiferromagnets. Ferromagnets possess a net macroscopic magnetization that breaks time-reversal symmetry and produces spin-polarized electronic bands, enabling phenomena such as the anomalous Hall (AH) effect. In contrast, antiferromagnets host compensated magnetic moments, resulting in vanishing net magnetization and, in most cases, spin-degenerate electronic structures in momentum space. While ferromagnets have long dominated spintronics due to their ease of electrical detection and control, antiferromagnets offer advantages such as vanishing stray field, robustness against external magnetic fields, and ultrafast spin dynamics. Bridging these two paradigms has been a long-standing goal in condensed-matter physics. Recently, this dichotomy has been fundamentally expanded by the identification of altermagnetism, a distinct magnetic phase in which compensated collinear magnetic order coexists with a large momentum-dependent

spin splitting¹⁻⁸. In altermagnets, opposite spin sublattices are not related by inversion or translation symmetries. Instead, they are connected by other crystal symmetry operations, such as rotations, mirror reflections, glide planes, and screw axes, thereby resulting in vanishing net magnetization but spin-polarized band structures and finite Berry curvature, even when spin-orbit coupling (SOC) is negligible¹⁻⁸. These unique properties position altermagnets as a new platform for exploring magnetotransport phenomena beyond conventional ferromagnets and antiferromagnets¹⁻¹⁵.

Altermagnetic band splitting has been directly observed using angle-resolved photoemission spectroscopy (ARPES) measurements on several materials, including α -MnTe, CrSb, Rb-deintercalated V_2Te_2O , and KV_2Se_2O (refs.¹⁶⁻²⁵), providing unambiguous momentum-resolved evidence for this new magnetic order. Complementary electrical transport measurements have revealed a *spontaneous* AH effect in α -MnTe (ref.²⁶), indicating the presence of nonzero Berry curvature despite compensated magnetization. Unlike metallic CrSb (refs.²⁷⁻²⁹), α -MnTe is a semiconductor with a band gap of \sim 1.4 eV (refs.^{26,30-33}). It has emerged as a promising altermagnetic platform for semiconducting spintronic applications owing to its high *Néel* temperature near room temperature^{34,35}, large spin splitting on the order of \sim 100 meV (refs.^{16,17}), and excellent compatibility with molecular beam epitaxy (MBE) growth. However, to date, experimental reports on the AH effect in α -MnTe have exhibited strong sample dependence^{26,36-43}, including sign reversals and temperature-restricted behavior, leaving the microscopic origin of the AH response in α -MnTe unresolved.

In this work, we employ MBE to grow *d*-unit-cell (UC) thick α -MnTe films on lattice-matched InP(111)A substrates. ARPES measurements reveal a large spin splitting of \sim 230 meV for the bulk valence band near the Fermi level, directly confirming the altermagnetic band structure. Importantly, we identify surface states that cross the Fermi surface and dominate the low-energy

electronic band structure. Electrical transport measurements uncover a robust AH effect persisting down to 2 K and a pronounced sign reversal near 175 K. The longitudinal resistance of α -MnTe films shows a weak thickness dependence for $d \geq 5$, indicating surface-dominated conduction. By systematically varying film thickness, growth conditions, and interfacial structure, we identify two competing AH contributions of opposite signs, which we attribute to distinct surface channels at the top Te-capping/MnTe and bottom MnTe/InP interfaces. Our first-principles calculations identify distinct surface states at these two interfaces with opposite AH conductivity and reveal their intimate connection to the bulk altermagnetic order. These findings establish interface engineering as a key mechanism for inducing Berry curvature and generating the AH effect in α -MnTe, providing a unified explanation that reconciles seemingly inconsistent results from prior experiments^{26,36-39}.

α -MnTe crystallizes in a hexagonal NiAs-type structure with space group $P6_3/mmc$. The adjacent Te atomic layers are related by a mirror operation M_z or a nonsymmorphic screw-axis rotation $C_{6z}t_{1/2}$, where $t_{1/2}$ denotes a half-UC translation along the c axis, rather than by inversion P or translation $t_{1/2}$ alone (Fig. 1a,b). When the spin configuration is taken into account, M_z or $C_{6z}t_{1/2}$ relates opposite spin sublattices, giving rise to a g -wave spin splitting even in the absence of SOC (refs.^{2-4,16}). When the in-plane magnetic moments align with the next-nearest-neighbor Mn-Mn direction, a finite Berry curvature is allowed, enabling the AH effect²⁶. As noted above, although the AH effect has been reported in α -MnTe films and single crystals, its microscopic origin remains debated^{26,36-43}. Positive AH resistance with a soft ferromagnetic-like hysteresis loop has been observed in MBE-grown α -MnTe films at $T \sim 150$ K (refs.^{26,36-38}), whereas MnTe single crystals exhibit highly sample-dependent AH behavior, with reported AH signs that are positive, negative, or even reversed⁴⁰⁻⁴³. Moreover, for MBE-grown α -MnTe films, the AH effect is

prominent only for $150 \text{ K} < T < 250 \text{ K}$ and strongly suppressed at lower temperatures^{26,36-38}, raising the possibility that extrinsic factors, such as structural anomaly or excess Mn dopants, rather than intrinsic Berry curvature of the bulk altermagnetic ground state, may play a dominant role^{36,37}.

We first optimize the MBE growth recipes of α -MnTe films on InP(111)A substrates ([Supplementary Information](#)) and then perform systematic structural characterizations. The lattice constant of InP is $a_0 = 0.590 \text{ nm}$. For the InP(111)A surface, the corresponding in-plane lattice parameter $a_0/\sqrt{2} \sim 0.417 \text{ nm}$ closely matches that of α -MnTe ($a = 0.416 \text{ nm}$). Due to the excellent lattice compatibility, sharp and streaky reflection high-energy electron diffraction (RHEED) patterns are observed throughout the MBE growth process ([Fig. S1](#)). Cross-sectional scanning transmission electron microscopy (STEM) image of a $d = 20$ film reveals an atomically sharp interface between MnTe and InP(111)A ([Fig. 1c](#)). In addition, STEM measurements show that the first few Te capping layers form an atomically sharp interface with the MnTe film ([Fig. S4b](#)). Atomic force microscopy image of an uncapped $d = 40$ film reveals a uniform surface morphology with a root-mean-square roughness of $\sim 0.856 \text{ nm}$ ([Fig. 1d](#)). Neutron diffraction measurements performed on a $d = 230$ film show the emergence of the (001) magnetic Bragg peak for $T < 300 \text{ K}$, confirming the onset of antiferromagnetic coupling between the two Mn sublattices ([Fig. 1e](#)). Fitting the T dependence of the peak intensity yields a *Néel* temperature $T_N = 303.9 \pm 0.5 \text{ K}$. X-ray diffraction measurements on a $d = 140$ film confirm the α -MnTe phase ([Fig. 1f](#)), and the rocking curve of the MnTe (004) diffraction peak exhibits a full width at half maximum (FWHM) of $\sim 0.18^\circ$, indicating excellent epitaxial growth of α -MnTe on InP(111)A ([Fig. 1g](#)). The coexistence of the NiAs-type lattice and the A-type antiferromagnetic structure satisfies the essential symmetry requirements for altermagnetic order, specifically, broken PT symmetry and the absence of anti-translation $t_{1/2}T$ symmetry, thereby establishing our MBE-grown MnTe films

as an ideal platform for exploring the link between spin-split band structures and the AH effect^{2,3}.

Next, we perform ARPES measurements on a $d = 50$ nm film (Fig. 2) with a pristine surface. A photon energy $h\nu \sim 21.218$ eV corresponds to $k_z = 0$ (Fig. 2a), as established in prior studies^{16,17}.

Figure 2b shows the second-derivative Fermi surface and constant-energy contours of the MnTe film at binding energies $E_B \sim 0.1$ eV and $E_B \sim 0.2$ eV. At $E_B = 0$, the Fermi surface consists of two circular hole-like pockets centered at the Γ point (labeled α and α_1). As E_B increases, the areas of the α and α_1 pockets expand. In addition, six elliptical pockets surrounding the Γ point (labeled β_1) emerge, with their long axes aligned along the Γ -K direction. The band dispersion measured along the K- Γ -K direction reveals two bands (β_1 and β_2) crossing at the Γ point near the Fermi level (Fig. 2c). Weak surface states α and α_1 cross the Fermi level and are more clearly resolved in the second-derivative band map (Fig. 2g). Besides β_1 , β_2 , α , and α_1 bands, the ARPES band dispersion shows several broad hole-like bands at the Γ point, located at ~ 0.5 eV (labeled γ), ~ 1 eV (δ), and ~ 1.2 eV (ε) below the Fermi level (Fig. 2c). The α and α_1 bands originate from surface states, whereas all other bands are derived from bulk states. Both the bulk band structure and the surface states observed experimentally are well reproduced by our first-principles calculations on MnTe with a top Te termination (Fig. 2d,f,h). We next focus on the spin-split bands near the Fermi level. The second-derivative band map shows two well-separated β_1 and β_2 bands, with a maximum energy splitting ΔE of ~ 230 meV (Fig. 2e), much larger than the values reported in prior studies^{16,17}. This large splitting, arising from the interplay between altermagnetism and SOC, is well reproduced by our first-principles calculations (Fig. 2f) and identified as a direct manifestation of altermagnetism^{16,17}. The surface states α and α_1 are clearly resolved in the second-derivative band map with respect to the momentum of the band dispersion (Fig. 2g) and agree well with the calculated band structure (Fig. 2h). Therefore, our ARPES results provide compelling

momentum-resolved evidence for bulk altermagnetism in MBE-grown α -MnTe films on InP(111)A. Furthermore, these results indicate that transport is dominated by surface states rather than bulk bands, as the top bulk valence band lies ~ 80 meV below the Fermi level.

To probe the connection between bulk altermagnetism and the AH effect, we perform electrical transport measurements on α -MnTe films on InP(111)A with $1 \leq d \leq 230$. [Figure 3a](#) shows the T dependence of the sheet longitudinal resistance ρ_{xx} . For $d = 1$ and $d = 2$, ρ_{xx} exhibits insulating behavior and diverges at low T . In contrast, the $d = 5$ film shows a substantially reduced ρ_{xx} and a pronounced hump feature near $T \sim 280$ K, which is associated with the paramagnetic-to-antiferromagnetic phase transition (i.e., T_N). For films with $5 \leq d \leq 230$, ρ_{xx} exhibits only a weak dependence on d . In this regime, the films show a metallic T dependence over 50 K $< T < 280$ K, in stark contrast to the behavior expected for a doped semiconductor. Upon cooling towards $T = 50$ K, a metal-to-insulator transition is observed. [Figure 3b](#) shows the T dependence of the normalized longitudinal resistance $\rho_{xx,norm} = \rho_{xx}/\rho_{xx,min}$. A Kondo-like transport behavior, manifested as a logarithmic upturn in ρ_{xx} at low T (refs.⁴⁴⁻⁴⁷), is likely attributed to magnetic impurities, such as excess Mn dopants³⁷. We further define T_{min} as the temperature at which ρ_{xx} reaches its minimum and find that T_{min} increases monotonically with d ([Fig. 3c](#)). More experiments are required to clarify the microscopic origin of the d -dependent T_{min} behavior observed in these MBE-grown α -MnTe films. [Figure 3d](#) shows the d dependence of ρ_{xx} measured at $T = 2$ K [denoted as $\rho_{xx}(T=2K)$]. A pronounced reduction in $\rho_{xx}(T=2K)$ is observed as d increases from 1 to 5, followed by a nearly saturated behavior for $d \geq 5$. The weak d dependence of $\rho_{xx}(T=2K)$, together with its slight increase at larger d indicates that electrical transport in MBE-grown α -MnTe films on InP(111)A is dominated by surface states rather than bulk states³⁶. The surface-dominated conduction is consistent with our ARPES results, which show that only the α and α_1 surface states

cross the Fermi level (Fig. 2b,c,g).

Next, we investigate the magnetotransport properties of the $d = 230$ film. For $250 \text{ K} \leq T \leq 300 \text{ K}$, the sample exhibits a linear Hall trace (Fig. S10). Upon further cooling, a soft hysteresis loop emerges at $T = 200 \text{ K}$ and persists down to $T = 2 \text{ K}$. Figure 4a shows the out-of-plane magnetic field $\mu_0 H$ dependence of the Hall resistance ρ_{yx} for $T \leq 200 \text{ K}$, after subtracting the linear contribution from the ordinary Hall effect. At $T = 200 \text{ K}$, the zero magnetic field Hall resistance $\rho_{yx}(0)$ after a positive magnetic field training is $\sim 2.94 \Omega$. As T decreases to $T = 150 \text{ K}$, $\rho_{yx}(0)$ switches sign and becomes $\sim -4.47 \Omega$. The AH sign reversal occurs for $150 \text{ K} < T < 200 \text{ K}$, and the shape of the AH hysteresis loop for $T \leq 150 \text{ K}$ indicates the coexistence of the two AH contributions with opposite AH signs in the $d = 230$ film⁴⁸⁻⁵². As T further decreases, $\rho_{yx}(0)$ decreases monotonically, reaching -7.71Ω at $T = 100 \text{ K}$, -10.45Ω at $T = 40 \text{ K}$, and -23.44Ω at $T = 2 \text{ K}$. At $T = 2 \text{ K}$, the Hall trace evolves into a sharp hysteresis loop with a small residual hump feature near the large coercive field $\mu_0 H_c \sim \pm 6.0 \text{ T}$, reflecting the hard ferromagnet-like nature of the $d = 230$ film. All these observations indicate that the positive AH component dominates for $T \geq 200 \text{ K}$. In contrast, the negative AH component becomes dominant for $T = 2 \text{ K}$. For $2 \text{ K} < T < 200 \text{ K}$, the positive and negative AH components compete. Their opposite AH signs and distinct $\mu_0 H_c$ suggest that they may arise from two opposite surfaces.

To further clarify the evolution of the AH effect, we examine the $\mu_0 H$ dependence of ρ_{yx} for $\alpha\text{-MnTe}$ films with $5 \leq d \leq 230$ at $T = 2 \text{ K}$ (Fig. 4b) and $T = T^*$ (Fig. 4c). Here, we define T^* as the temperature at which the positive $\rho_{yx}(0)$ reaches its maximum (Fig. 4d). At $T = 2 \text{ K}$, a well-defined hysteresis loop with a negative AH sign is observed for $d \geq 20$. In contrast, it gradually shrinks as d decreases and becomes negligible for $d = 10$ and $d = 5$. $\rho_{yx}(0)$ at $T = 2 \text{ K}$ [denoted as

$\rho_{yx}(0)(T=2\text{K})$] is found to be $\sim -23.4 \Omega$ for $d = 230$, $\sim -22.3 \Omega$ for $d = 40$, and $\sim -13.5 \Omega$ for $d = 20$ (Fig. 4b). In contrast, a pronounced hysteresis loop with a positive AH sign is observed for all samples at $T = T^*$, while it gradually expands as d decreases. $\rho_{yx}(0)$ at $T = T^*$ [denoted as $\rho_{yx}(0)(T=T^*)$] is found to be $\sim 2.9 \Omega$ for $d = 230$, $\sim 7.4 \Omega$ for $d = 40$, $\sim 8.6 \Omega$ for $d = 20$, $\sim 22.3 \Omega$ for $d = 10$, and $\sim 41.3 \Omega$ for $d = 5$ (Fig. 4c). As d increases from 2 to 230, the appearance of a hysteresis loop with a negative AH sign at $T = 2 \text{ K}$, together with the suppression of a hysteresis loop with a positive AH sign at $T = T^*$, further indicates the presence of two competing AH contributions with opposite AH signs in our MBE-grown α -MnTe films on InP(111)A. Figure 4d shows the T dependence of $\rho_{yx}(0)$ for α -MnTe films with $1 \leq d \leq 230$. For $d = 230$ and $d = 40$, $\rho_{yx}(0)$ becomes finite at $T \sim 225 \text{ K}$. It reaches a maximum at $T^* = 200 \text{ K}$. Upon further cooling, $\rho_{yx}(0)$ reverses sign at $T \sim 175 \text{ K}$ and then decreases monotonically as T decreases. For $d = 20$, T^* remains at 200 K, while $\rho_{yx}(0)$ reverses sign at $T \sim 50 \text{ K}$. For $d \leq 10$, the positive AH component is significantly enhanced, whereas the negative AH component is strongly suppressed at low temperatures. $\rho_{yx}(0)$ reaches its maximum at $T^* = 260 \text{ K}$ for $d = 10$, $T^* = 250 \text{ K}$ for $d = 5$, and $T^* = 175 \text{ K}$ for $d = 2$, respectively. In contrast, for $d = 1$, no AH effect is observed, indicating the absence of long-range magnetic order in a single UC α -MnTe layer (Fig. 4d).

Finally, we verify the surface-state origin of the AH effect using first-principles calculations. We first construct a slab model for a MnTe film on an InP(111)A substrate with a Te capping layer (Fig. 5a). By identifying the surface states on the top and bottom surfaces, we evaluate their contributions to σ_{xy} (Fig. 5b-d). At the bottom surface, MnTe bonds to the InP substrate via interfacial Te atoms, whereas the top surface is Te-terminated as confirmed by the consistency between our ARPES measurements and first-principles calculations (Fig. 2g,h). The Te capping layer is modeled by adding an extra Te layer on the top Te-terminated surface (Supplementary

Information). The resulting top and bottom surface states are highlighted by dotted lines in Fig. 5c,d. We note that the Te capping layer modifies the surface band structure, resulting in deviations from the ARPES measurements of pristine MnTe (Fig. 2g). In our first-principles calculations, the charge neutral point is fixed at $E = 0$ eV, and the experimental E_F determined from ARPES is slightly above the bulk bands, at $E \sim -0.2$ eV. At $E \sim -0.2$ eV, the top Te/MnTe and bottom MnTe/InP surface bands contribute $-8.4 \mu\text{S}$ and $+0.7 \mu\text{S}$ to σ_{xy} , respectively (Fig. 5b). The calculated surface σ_{xy} is on the order of $1 \mu\text{S}$, in good agreement with the experimentally extracted values of $-2 \mu\text{S} < \sigma_{xy} < 2 \mu\text{S}$ (Fig. S17a). In contrast, even taking the upper bound of the reported bulk σ_{xy} of $\sim 10^{-2}$ S/cm (ref.⁴¹), this corresponds to $\sim 6.71 \times 10^{-4} \mu\text{S}$ per UC in 2D. To reach $\sigma_{xy} \sim 1 \mu\text{S}$, a minimum thickness of $d \sim 1500$ would be required, far exceeding the thickness of all MnTe films with $1 \leq d \leq 230$ studied in this work. Therefore, we demonstrate that the AH response in our MnTe films is dominated by surface state contributions, even if the bulk is doped. To probe the sensitivity to the surface environment, we passivate the top surface with hydrogen atoms to simulate oxidation, the top surface states shift downward into the bulk bands and away from E_F , whereas the bottom surface states remain unchanged (Fig. S6). This behavior is consistent with the experimental observation that positive and negative AH components coexist and are highly sensitive to interfacial environment (Supplementary Information). Moreover, because our MnTe films are in the strong-disorder regime, with low carrier mobility $\mu < 100 \text{ cm}^2 \cdot \text{V}^{-1} \cdot \text{s}^{-1}$ (Fig. S17c), extrinsic AH mechanisms are strongly suppressed, indicating that the observed AH effect in our MnTe films is predominantly intrinsic from the band Berry curvature⁵³.

The surface-state-driven AH effect is an intrinsic manifestation of bulk altermagnetism, even though the bulk bands do not cross E_F . Our first-principles calculations show that, for a fixed Te/MnTe or MnTe/InP interface structure, the AH sign is independent of the magnetization

direction of the surface MnTe layer and instead governed by the bulk altermagnetic order. To explicitly demonstrate this, we focus on the top Te/MnTe interface and compare three different MnTe termination configurations (i), (ii), and (iii) in [Fig. 5e](#). Configurations (i) and (ii) share the same bulk altermagnetic order (see dashed black boxes in [Fig. 5e](#)) but are terminated at different MnTe layers with opposite magnetization directions. Because these two configurations can be related by the two-fold rotation C_{2z} , which preserves σ_{xy} , they exhibit the same σ_{xy} . In contrast, Configurations (i) and (iii) have opposite bulk altermagnetic orders but are terminated at the MnTe layer with the same magnetization direction. We find these two configurations have opposite σ_{xy} , since they are related by the combined $C_{2z}T$ symmetry. This symmetry-based comparison unambiguously demonstrates that the AH sign is determined by the bulk altermagnetic order, rather than by the magnetization direction of the surface MnTe layer, even though the AH effect originates from the top and bottom surface layers.

To summarize, we demonstrate the surface-state-driven AH effect in MBE-grown α -MnTe films on InP(111)A that host bulk altermagnetism. A spin-split band structure induced by bulk altermagnetism is observed, with an energy splitting of ~ 230 meV well below the Fermi level. We find that the Fermi level is crossed exclusively by surface states. Consistent with this observation, electrical transport measurements indicate surface-dominated conduction. By systematically varying film thickness, growth conditions, and interfacial structure, we identify two competing AH contributions with opposite AH signs, originating from distinct surface channels at the top Te/MnTe and bottom MnTe/InP interfaces. Our first-principles calculations confirm the coexistence of these two surface channels and reveal that their AH contributions are governed by the combined effects of surface/interface chemical environment and bulk altermagnetism, rather than the magnetization direction of the surface MnTe layer. These findings establish a surface-

sensitive probe of bulk altermagnetism, demonstrate interface engineering as an effective route to inducing the AH effect in MBE-grown α -MnTe films, and lay the foundation for the development of altermagnet-based electronic and spintronic devices.

Methods

MBE growth

All MnTe films are grown on 0.35-mm-thick insulating InP(111)A substrates in a commercial MBE chamber (Omicron Lab 10) with a base pressure of $\sim 2.0 \times 10^{-10}$ mbar. Before MBE growth, the InP(111)A substrates are first degassed at ~ 500 °C under a Te flux for 30 mins. High-purity Mn (99.9998%) and Te (99.9999%) are evaporated from two Knudsen effusion cells. During MBE growth, the InP(111)A substrate temperature is maintained at ~ 330 °C. The growth rate of MnTe is ~ 0.15 UC/min. After MBE growth, the MnTe films are capped with a 10-nm-thick Te layer at room temperature to prevent oxidation during ex situ measurements.

Electrical transport measurements

The MnTe films used for electrical transport measurements are patterned into Hall bar devices by mechanical scratching using a computer-controlled probe station. The effective Hall bar area is ~ 1 mm \times 0.5 mm. Electrical contacts are made by pressing indium dots on the film surface. Electrical transport measurements are performed in two Physical Property Measurement Systems (Quantum Design DynaCool, 2 K, 9 T and 2 K, 14 T). An excitation current of ~ 10 μ A is applied by a Keithley 6221 current source, and the voltage is measured using a Stanford Research Systems SR860 lock-in amplifier. The magnetotransport results shown in the main text and [Supplementary Information](#) are symmetrized or antisymmetrized with respect to the magnetic field to eliminate artifacts arising from electrode misalignment.

ARPES measurements

In situ ARPES measurements are performed in a chamber with a base vacuum of $\sim 5 \times 10^{-11}$ mbar. The MBE-grown MnTe films are transferred to the ARPES chamber without breaking the ultrahigh vacuum. A helium discharge lamp (He-I_α , $h\nu = 21.218$ eV) is used as the photon source. The energy resolution is ~ 10 meV, and the angular resolution is $\sim 0.1^\circ$.

First-principles calculations

First-principles calculations are performed with the Vienna Ab initio Simulation Package (VASP) using the projector-augmented wave method⁵⁴. The exchange-correlation functional is treated with generalized gradient approximation (GGA) using the Perdew-Burke-Ernzerhof (PBE) parametrization⁵⁵. Brillouin zone integrations are performed by using Γ -centered k -point meshes of $12 \times 12 \times 10$ for bulk MnTe and $12 \times 12 \times 1$ for the MnTe-InP slab. In the slab calculations, atomic positions are fully relaxed while fixing the in-plane lattice constants. We employ the DFT + U method⁵⁶ with the on-site Coulomb interaction $U = 4.80$ eV and exchange interaction $J = 0.80$ eV for Mn (ref.¹⁶). Maximally localized Wannier functions are constructed using the Wannier90 package⁵⁷, including Mn- s, d , Te- p , In- s, p , P- p , and H- s orbitals. Surface states of the MnTe films are obtained from a semi-infinite slab with Te termination using the recursive Green's function. The AH conductance σ_{xy} is calculated by integrating the Kubo formula over a 400×400 k -mesh.

To demonstrate surface-dominated transport in MnTe films, we construct a slab model consisting of 14 MnTe atomic layers (i.e., $d = 7$) and 8 InP atomic layers, which suppresses hybridization between the top and bottom surfaces in the ultrathin limit. Based on this slab structure, a Wannier-based tight-binding model is built to treat both the MnTe/InP interface and the top surface, with and without Te capping layers, and used to compute σ_{xy} . To resolve the atomic layer contribution to σ_{xy} , we project the Berry curvature onto each atomic layer⁵⁸

$$\sigma_{xy}(l) = \frac{e^2}{\hbar} \sum_n \int \frac{d^2 k}{(2\pi)^2} f(\varepsilon_n) \Omega_n^{xy}(\mathbf{k}, l), \quad (1)$$

where $\Omega_n^{xy}(\mathbf{k}, l)$ is the layer-projected Berry curvature of band n ,

$$\Omega_n^{xy}(\mathbf{k}, l) = -2\text{Im} \sum_{m \neq n} \frac{\langle n | \hat{P}_l \partial_{k_x} H | m \rangle \langle m | \partial_{k_y} H | n \rangle}{(\varepsilon_n - \varepsilon_m)^2}, \quad (2)$$

Here $\hat{P}_l = |l\rangle\langle l|$ is the projector onto the l^{th} atomic layer. To suppress numerical fluctuations in the bulk region caused by the reduced symmetry of the slab Hamiltonian, a sliding-average smoothing procedure is applied along the layer index. Specifically, for the 10th to 22nd layers in [Figs. S6](#) and [S7](#), each smoothed value is computed as the average over four consecutive layers, corresponding to 1 UC: $\bar{\sigma}_{xy}(l) = \frac{1}{4} \sum_{k=0}^3 \sigma_{xy}(l+k)$. Layers outside this range, including the top surface and interface regions, are not smoothed.

Neutron diffraction measurements

Neutron diffraction measurements are performed using the WISH diffractometer at the ISIS Neutron and Muon Source⁵⁹. The MnTe films are wrapped in an aluminum foil and mounted on an aluminum strip, with the MnTe H0L plane aligned in the scattering plane. Temperature-dependent measurements are performed in a helium-flow cryostat. The raw neutron diffraction data are reduced and analyzed using the Mantid software package⁶⁰.

Reflective magnetic circular dichroism (RMCD) measurements

RMCD measurements are performed using a 633 nm laser. The incident beam is intensity-modulated by an optical chopper and passed through a photoelastic modulator to alternate between left- and right-handed circular polarizations. The sample is mounted in a Quantum Design OptiCool cryostat, with the magnetic field applied along the optical axis in a Faraday geometry. In

this configuration, the RMCD signal is primarily sensitive to the out-of-plane component of the magnetization. The reflected light is detected by a photodiode, and the output is demodulated using lock-in amplifier detection. One lock-in channel is referenced to the photoelastic modulator to obtain the differential reflectance between opposite circular polarizations, while a second channel is referenced to the chopper to measure the average reflectance. The RMCD signal is calculated as the differential reflectance normalized by the average reflectance.

Acknowledgments: We thank C. Du, N. Samarth, W. Wu, D. Xiao, and J. Zhu for helpful discussions. This project is primarily supported by the ONR Award (N000142412133), including MBE growth and PPMS(9T) measurements. ARPES and PPMS(14T) measurements and theoretical calculations are supported by the seed project of the Penn State MRSEC for Nanoscale Science (DMR-2011839). Sample characterization is supported by the NSF grant (DMR-2241327) and the ARO award (W911NF2210159). TA, GPT, and ZL acknowledge start-up support from Binghamton University. Partial support for AJG is provided by the Center for High Resolution Neutron Scattering, a partnership between the NIST and the NSF under Agreement No. DMR-2010792. B.Y. acknowledges the support by the Israel Science Foundation (ISF: 2974/23). Certain commercial equipment, instruments, software, or materials are identified in this paper to specify the experimental procedure adequately. Such identifications are not intended to imply recommendation or endorsement by NIST, nor are they intended to imply that the materials or equipment identified are necessarily the best available for the purpose. The authors acknowledge the Science and Technology Facility Council (STFC), part of UKRI, for the provision of beam time on the WISH diffractometer under proposal No. RB2510207. CZC acknowledges the support from the Gordon and Betty Moore Foundation’s EPiQS Initiative (GBMF9063 to C. -Z. C).

Author contributions: CZC conceived and designed the experiment. LJZ, ZJY, PX, LKL, ZX,

and CZC performed the MBE growth and conducted electrical transport measurements. HR, ZJY, PX, and CZC performed all ARPES measurements. LJZ, ZJY, PX, LKL, and CZC performed the atomic force microscopy and XRD measurements. LJZ, ZJY, PX, and KW performed STEM measurements. PM, FO, DK, and AJG performed neutron diffraction measurements. TA, GPT, and ZL performed RMCD measurements. YZ, CXL, and BY provided theoretical support. LJZ, HR, YZ, CXL, BY, and CZC analyzed the data and wrote the manuscript with input from all authors.

Competing interests: The authors declare no competing financial interests.

Data availability: The data that support the findings of this article are openly available⁶¹.

Figures and figure captions:

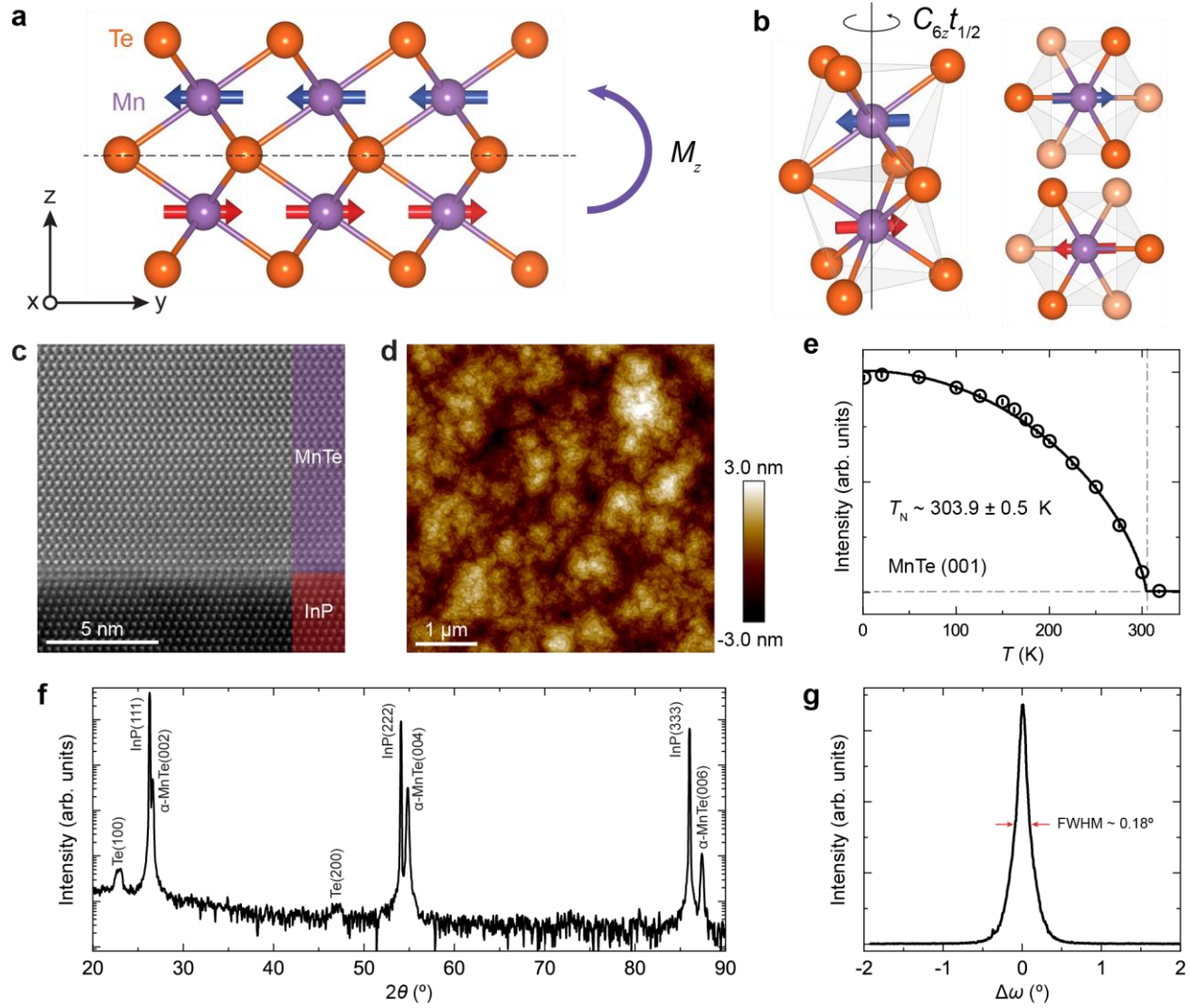


Fig. 1 | Characterization of epitaxial MnTe films on InP(111)A substrates. **a, b**, Crystal and magnetic structure of MnTe. M_z or $C_{6z}t_{1/2}$ relates opposite spin sublattices. M_z is the mirror operation with the basal plane (001). C_{6z} is a six-fold rotation operation, and $t_{1/2}$ is a half-UC translation along the c -axis. **c**, STEM image of a $d = 20$ nm film. **d**, Atomic force microscope image taken on an uncapped $d = 20$ nm film. **e**, T -dependent (001) peak intensity of a $d = 230$ nm film measured by neutron diffraction. The fit yields $T_N = 303.9 \text{ K} \pm 0.5 \text{ K}$. Error bars represent ± 1 standard deviation. **f**, XRD spectrum of a $d = 140$ nm film. **g**, Corresponding rocking curve of the MnTe (004) peak with a FWHM of $\sim 0.18^\circ$.

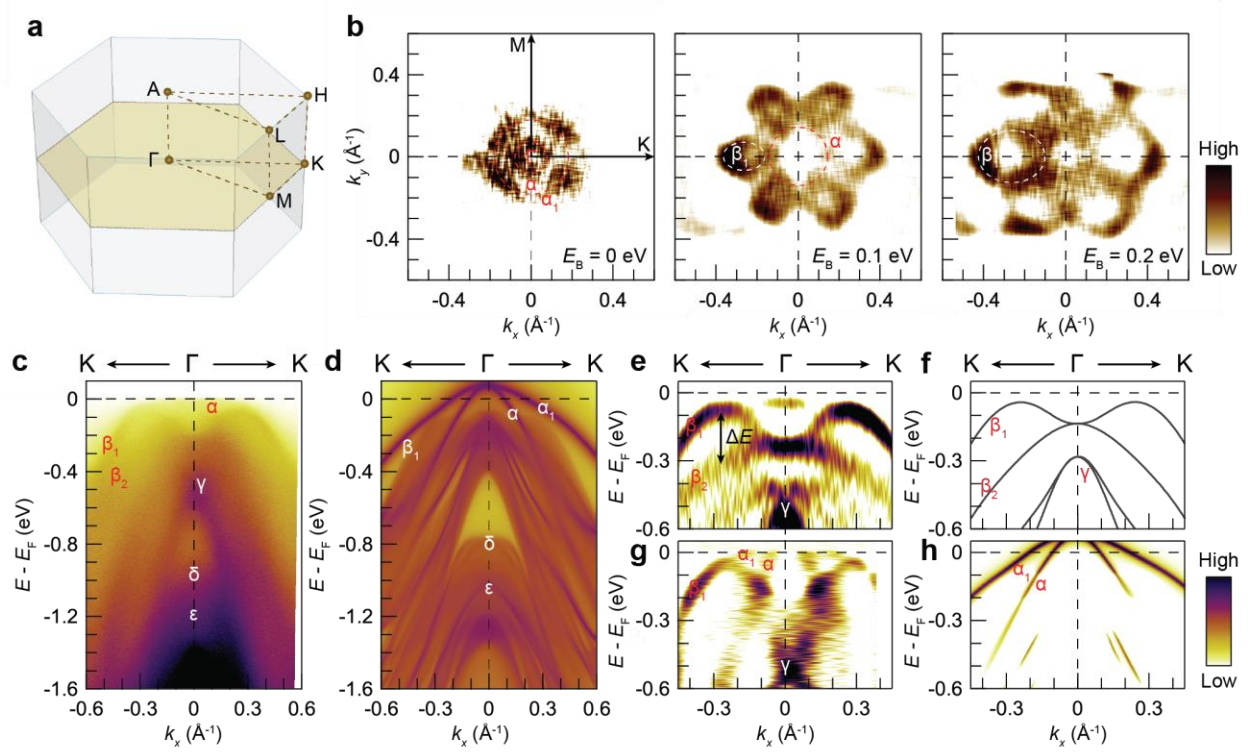


Figure 2| Surface states and spin-split bands in epitaxial MnTe films with $d = 50$. **a**, 3D Brillouin zone of MnTe. The yellow plane indicates the $k_z = 0$ plane. **b**, Second derivative constant-energy contours at Fermi surface (left), $E_B = 0.1$ eV (middle), and $E_B = 0.2$ eV (right). The second-derivative Fermi surface is obtained by integrating the spectral weight within a [-25, 25] meV window, and the other second-derivative constant-energy contours are obtained by integrating the spectral weight within a [-20, 20] meV window with respect to the corresponding E_B . **c**, ARPES band dispersion measured along the K- Γ -K direction. **d**, Calculated surface states and bulk band structure of MnTe with a Te-terminated top surface along the K- Γ -K direction in the altermagnetic state with SOC. Strong spectrum weight indicates surface states, and weak broad regions are bulk bands. **e**, The second-derivative band map with respect to the energy of the band structure. **f**, Calculated bulk band structure along the K- Γ -K direction. **g**, The second-derivative band map with respect to the momentum of the band structure. **h**, The same calculated electronic band structure in (d), shown with a different color scale to highlight the surface states (α and α_1). All ARPES measurements are performed at $T = 12$ K.

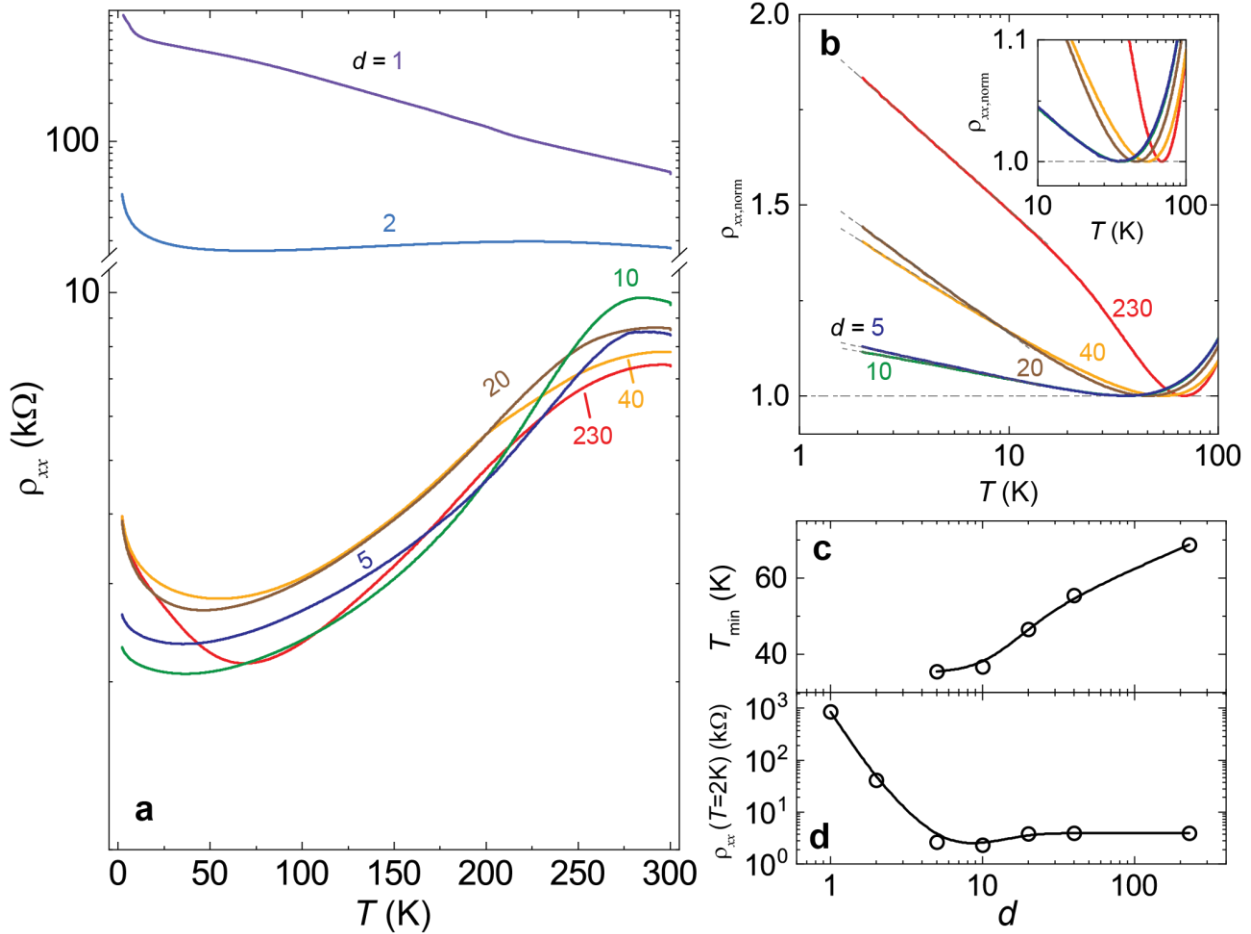


Fig. 3| Surface conduction in epitaxial MnTe films. **a**, T -dependent ρ_{xx} of MnTe films with $d = 1, 2, 5, 10, 20, 40$, and 230 . **b**, T dependence of the normalized $\rho_{xx}/\rho_{xx,\text{min}}$ for MnTe films with $d = 5, 10, 20, 40$, and 230 . Inset: Enlarged view near $\rho_{xx,\text{min}}$. The dashed lines indicate the logarithmic increase at low T . **c**, d dependence of T_{min} , defined as the temperature at which ρ_{xx} reaches its minimum. **d**, d dependence of $\rho_{xx}(T=2\text{K})$.

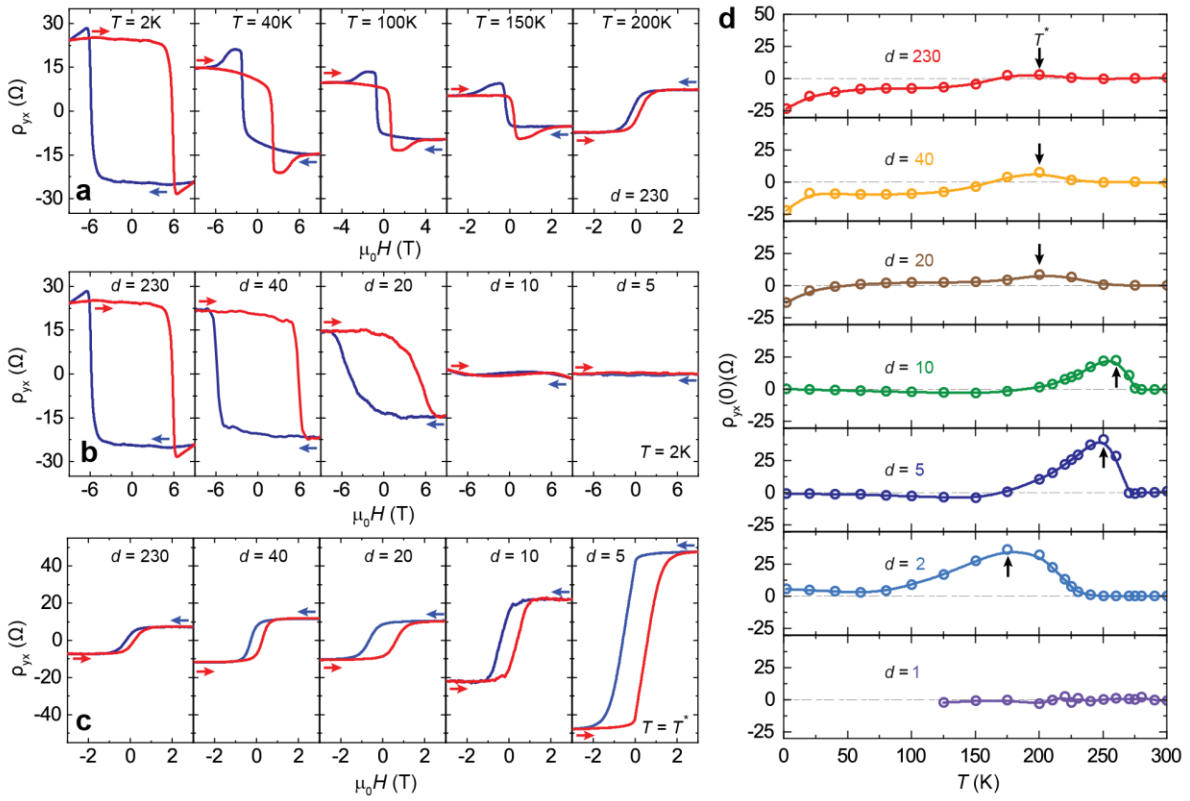


Fig. 4| d -dependent AH effect in epitaxial MnTe films. **a**, $\mu_0 H$ -dependent ρ_{yx} measured at $T = 2$ K, 40 K, 100 K, 150 K, and 200 K for a MnTe film with $d = 230$. **b**, **c**, $\mu_0 H$ -dependent ρ_{yx} for MnTe films with $d = 230, 40, 20, 10$, and 5 measured at $T = 2$ K (**b**) and $T = T^*$ (**c**). T^* denotes the temperature at which $\rho_{yx}(0)$ reaches its maximum. **d**, T dependence $\rho_{yx}(0)$ for MnTe films with $d = 1, 2, 5, 10, 20, 40$, and 230. The arrows indicate the T^* values.

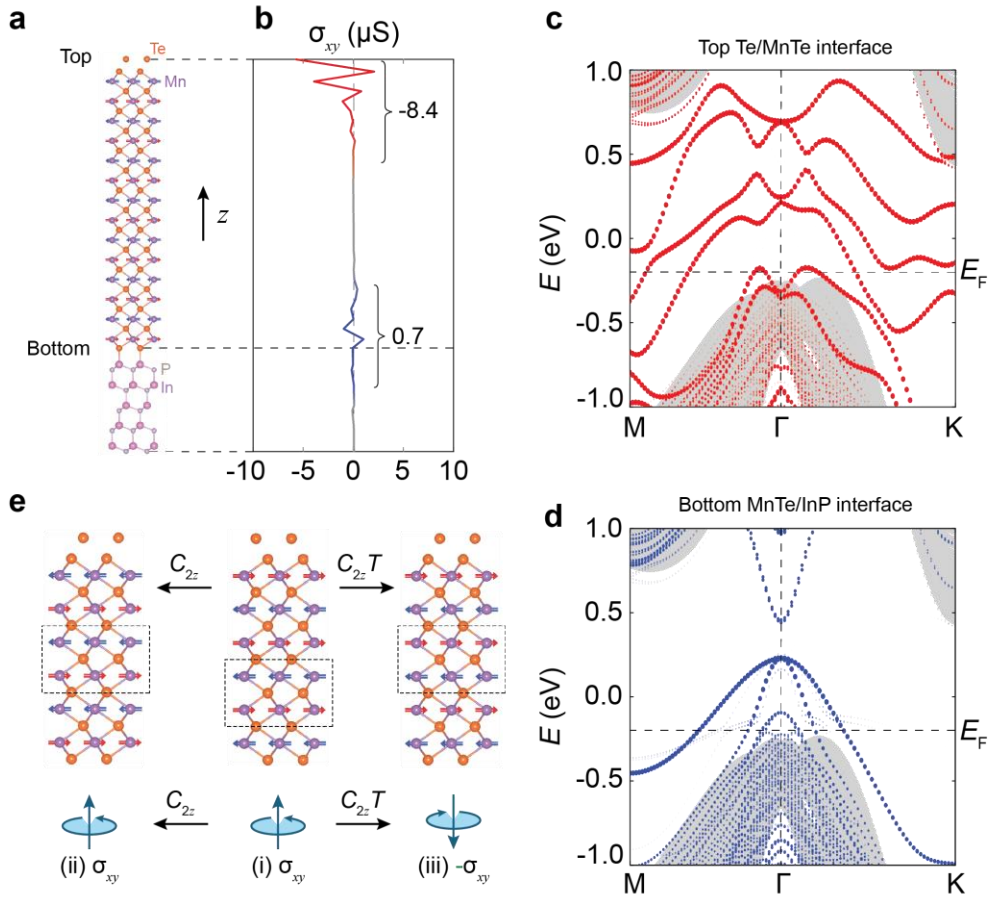


Fig. 5 | Surface-state-driven AH effect and bulk altermagnetism in MnTe films. **a**, Schematic of a MnTe film with $d = 7$ on an InP substrate with a Te capping layer. **b**, Layer-projected σ_{xy} along the z direction calculated at E_F . The top and bottom regions contribute $-8.4 \mu\text{S}$ and $+0.7 \mu\text{S}$ to σ_{xy} , respectively. E_F is indicated by the dashed line in **c**, **d**. **c**, Projected band structure of the top Te/MnTe interface. **d**, Projected band structure of the bottom MnTe/InP interface. The grey shadow in **c**, **d** is the bulk states. E_F is set at $E \sim -0.2 \text{ V}$, as determined from ARPES measurements. **e**, Schematic of the MnTe film (i) and its symmetry-related counterparts under the C_{2z} (ii) and $C_{2z}T$ (iii) operations. σ_{xy} , as a pseudovector along the z direction, is invariant under C_{2z} but changes sign under $C_{2z}T$. C_{2z} denotes the two-fold rotation operation in the magnetic space group, and T is the time-reversal operation. The bulk altermagnetic order is highlighted in the dashed boxes. Configurations (i) and (ii) share the same altermagnetic order and σ_{xy} , despite reversed magnetization in the terminated MnTe layer, whereas Configurations (i) and (iii) have the same surface magnetization but have opposite bulk altermagnetic order and σ_{xy} .

References:

- 1 Šmejkal, L., González-Hernández, R., Jungwirth, T. & Sinova, J. Crystal time-reversal symmetry breaking and spontaneous Hall effect in collinear antiferromagnets. *Sci. Adv.* **6**, eaaz8809 (2020).
- 2 Šmejkal, L., Sinova, J. & Jungwirth, T. Beyond Conventional Ferromagnetism and Antiferromagnetism: A Phase with Nonrelativistic Spin and Crystal Rotation Symmetry. *Phys. Rev. X* **12**, 031042 (2022).
- 3 Šmejkal, L., Sinova, J. & Jungwirth, T. Emerging Research Landscape of Altermagnetism. *Phys. Rev. X* **12**, 040501 (2022).
- 4 Song, C., Bai, H., Zhou, Z., Han, L., Reichlova, H., Dil, J. H., Liu, J., Chen, X. & Pan, F. Altermagnets as a new class of functional materials. *Nat. Rev. Mater.* **10**, 473 (2025).
- 5 Jungwirth, T., Sinova, J., Fernandes, R. M., Liu, Q., Watanabe, H., Murakami, S., Nakatsuji, S. & Šmejkal, L. Symmetry, microscopy and spectroscopy signatures of altermagnetism. *Nature* **649**, 837 (2026).
- 6 Jungwirth, T., Fernandes, R. M., Fradkin, E., MacDonald, A. H., Sinova, J. & Šmejkal, L. Altermagnetism: An unconventional spin-ordered phase of matter. *Newton* **1**, 100162 (2025).
- 7 Fender, S. S., Gonzalez, O. & Bediako, D. K. Altermagnetism: A Chemical Perspective. *J. Am. Chem. Soc.* **147**, 2257 (2025).
- 8 Mazin, I. Altermagnetism then and now. *Physics* **17**, 4 (2024).
- 9 Ma, H.-Y., Hu, M., Li, N., Liu, J., Yao, W., Jia, J.-F. & Liu, J. Multifunctional antiferromagnetic materials with giant piezomagnetism and noncollinear spin current. *Nat. Commun.* **12**, 2846 (2021).
- 10 Hayami, S., Yanagi, Y. & Kusunose, H. Bottom-up design of spin-split and reshaped electronic band structures in antiferromagnets without spin-orbit coupling: Procedure on the basis of augmented multipoles. *Phys. Rev. B* **102**, 144441 (2020).
- 11 Yuan, L.-D., Wang, Z., Luo, J.-W., Rashba, E. I. & Zunger, A. Giant momentum-dependent spin splitting in centrosymmetric low-Z antiferromagnets. *Phys. Rev. B* **102**, 014422 (2020).

12 Mali, S., Zhao, Y., Wang, Y., Sarker, S., Chen, Y., Li, Z., Zhu, J., Liu, Y., Gopalan, V. & Yan, B. Probing Hidden Symmetry and Altermagnetism with Sub-Picometer Sensitivity via Nonlinear Transport. *arXiv:2510.18144* (2025).

13 Mazin, I. I., Koepernik, K., Johannes, M. D., González-Hernández, R. & Šmejkal, L. Prediction of unconventional magnetism in doped FeSb₂. *Proc. Natl. Acad. Sci.* **118**, e2108924118 (2021).

14 Chen, X., Liu, Y., Liu, P., Yu, Y., Ren, J., Li, J., Zhang, A. & Liu, Q. Unconventional magnons in collinear magnets dictated by spin space groups. *Nature* **640**, 349 (2025).

15 Liu, P., Li, J., Han, J., Wan, X. & Liu, Q. Spin-Group Symmetry in Magnetic Materials with Negligible Spin-Orbit Coupling. *Phys. Rev. X* **12**, 021016 (2022).

16 Krempasky, J., Smejkal, L., D'Souza, S. W., Hajlaoui, M., Springholz, G., Uhlirova, K., Alarab, F., Constantinou, P. C., Strocov, V., Usanov, D., Pudelko, W. R., Gonzalez-Hernandez, R., Birk Hellenes, A., Jansa, Z., Reichlova, H., Soban, Z., Gonzalez Betancourt, R. D., Wadley, P., Sinova, J., Kriegner, D., Minar, J., Dil, J. H. & Jungwirth, T. Altermagnetic lifting of Kramers spin degeneracy. *Nature* **626**, 517 (2024).

17 Hajlaoui, M., Wilfred D'Souza, S., Smejkal, L., Kriegner, D., Krizman, G., Zakusylo, T., Olszowska, N., Caha, O., Michalicka, J., Sanchez-Barriga, J., Marmodoro, A., Vyborny, K., Ernst, A., Cinchetti, M., Minar, J., Jungwirth, T. & Springholz, G. Temperature Dependence of Relativistic Valence Band Splitting Induced by an Altermagnetic Phase Transition. *Adv. Mater.* **36**, 202314076 (2024).

18 Osumi, T., Souma, S., Aoyama, T., Yamauchi, K., Honma, A., Nakayama, K., Takahashi, T., Ohgushi, K. & Sato, T. Observation of a giant band splitting in altermagnetic MnTe. *Phys. Rev. B* **109**, 115102 (2024).

19 Lee, S., Lee, S., Jung, S., Jung, J., Kim, D., Lee, Y., Seok, B., Kim, J., Park, B. G., Šmejkal, L., Kang, C.-J. & Kim, C. Broken Kramers Degeneracy in Altermagnetic MnTe. *Phys. Rev. Lett.* **132**, 036702 (2024).

20 Lee, J.-E., Zhong, Y., Li, Q., Edmonds, M. T., Shen, Z.-X., Hwang, C. & Mo, S.-K.

Dichotomous Temperature Response in the Electronic Structure of Epitaxially Grown Altermagnet MnTe. *Nano Lett.* **25**, 8969 (2025).

21 Ding, J., Jiang, Z., Chen, X., Tao, Z., Liu, Z., Li, T., Liu, J., Sun, J., Cheng, J., Liu, J., Yang, Y., Zhang, R., Deng, L., Jing, W., Huang, Y., Shi, Y., Ye, M., Qiao, S., Wang, Y., Guo, Y., Feng, D. & Shen, D. Large Band Splitting in g-Wave Altermagnet CrSb. *Phys. Rev. Lett.* **133**, 206401 (2024).

22 Yang, G., Li, Z., Yang, S., Li, J., Zheng, H., Zhu, W., Pan, Z., Xu, Y., Cao, S., Zhao, W., Jana, A., Zhang, J., Ye, M., Song, Y., Hu, L.-H., Yang, L., Fujii, J., Vobornik, I., Shi, M., Yuan, H., Zhang, Y., Xu, Y. & Liu, Y. Three-dimensional mapping of the altermagnetic spin splitting in CrSb. *Nat. Commun.* **16**, 1442 (2025).

23 Reimers, S., Odenbreit, L., Šmejkal, L., Strocov, V. N., Constantinou, P., Hellenes, A. B., Jaeschke Ubiergo, R., Campos, W. H., Bharadwaj, V. K., Chakraborty, A., Denneulin, T., Shi, W., Dunin-Borkowski, R. E., Das, S., Kläui, M., Sinova, J. & Jourdan, M. Direct observation of altermagnetic band splitting in CrSb thin films. *Nat. Commun.* **15**, 2116 (2024).

24 Zhang, F., Cheng, X., Yin, Z., Liu, C., Deng, L., Qiao, Y., Shi, Z., Zhang, S., Lin, J., Liu, Z., Ye, M., Huang, Y., Meng, X., Zhang, C., Okuda, T., Shimada, K., Cui, S., Zhao, Y., Cao, G.-H., Qiao, S., Liu, J. & Chen, C. Crystal-symmetry-paired spin–valley locking in a layered room-temperature metallic altermagnet candidate. *Nat. Phys.* **21**, 760 (2025).

25 Jiang, B., Hu, M., Bai, J., Song, Z., Mu, C., Qu, G., Li, W., Zhu, W., Pi, H., Wei, Z., Sun, Y.-J., Huang, Y., Zheng, X., Peng, Y., He, L., Li, S., Luo, J., Li, Z., Chen, G., Li, H., Weng, H. & Qian, T. A metallic room-temperature d-wave altermagnet. *Nat. Phys.* **21**, 754 (2025).

26 Betancourt, R. D. G., Zubac, J., Gonzalez-Hernandez, R., Geishendorf, K., Soban, Z., Springholz, G., Olejnik, K., Smejkal, L., Sinova, J., Jungwirth, T., Goennenwein, S. T. B., Thomas, A., Reichlova, H., Zelezny, J. & Kriegner, D. Spontaneous Anomalous Hall Effect Arising from an Unconventional Compensated Magnetic Phase in a Semiconductor. *Phys. Rev. Lett.* **130**, 036702 (2023).

27 He, Q. L., Yin, G., Yu, L., Grutter, A. J., Pan, L., Chen, C.-Z., Che, X., Yu, G., Zhang, B.,

Shao, Q., Stern, A. L., Casas, B., Xia, J., Han, X., Kirby, B. J., Lake, R. K., Law, K. T. & Wang, K. L. Topological Transitions Induced by Antiferromagnetism in a Thin-Film Topological Insulator. *Phys. Rev. Lett.* **121**, 096802 (2018).

28 He, Q. L., Kou, X., Grutter, A. J., Yin, G., Pan, L., Che, X., Liu, Y., Nie, T., Zhang, B., Disseler, S. M., Kirby, B. J., Ratcliff II, W., Shao, Q., Murata, K., Zhu, X., Yu, G., Fan, Y., Montazeri, M., Han, X., Borchers, J. A. & Wang, K. L. Tailoring exchange couplings in magnetic topological-insulator/antiferromagnet heterostructures. *Nat. Mater.* **16**, 94 (2017).

29 Zhou, Z., Cheng, X., Hu, M., Chu, R., Bai, H., Han, L., Liu, J., Pan, F. & Song, C. Manipulation of the altermagnetic order in CrSb via crystal symmetry. *Nature* **638**, 645 (2025).

30 Kriegner, D., Vyborny, K., Olejnik, K., Reichlova, H., Novak, V., Marti, X., Gazquez, J., Saidl, V., Nemec, P., Volobuev, V. V., Springholz, G., Holý, V. & Jungwirth, T. Multiple-stable anisotropic magnetoresistance memory in antiferromagnetic MnTe. *Nat. Commun.* **7**, 11623 (2016).

31 Ferrer-Roca, C., Segura, A., Reig, C. & Muñoz, V. Temperature and pressure dependence of the optical absorption in hexagonal MnTe. *Phys. Rev. B* **61**, 13679 (2000).

32 Zanmarchi, G. Optical measurements on the antiferromagnetic semiconductor MnTe. *J. Phys. Chem. Solids* **28**, 2123 (1967).

33 Allen, J. W., Lucovsky, G. & Mikkelsen, J. C. Optical properties and electronic structure of crossroads material MnTe. *Solid State Commun.* **24**, 367 (1977).

34 Szuszkiewicz, W., Hennion, B., Witkowska, B., Łusakowska, E. & Mycielski, A. Neutron scattering study of structural and magnetic properties of hexagonal MnTe. *Phys. Status Solidi (c)* **2**, 1141 (2005).

35 Kriegner, D., Reichlova, H., Grenzer, J., Schmidt, W., Ressouche, E., Godinho, J., Wagner, T., Martin, S. Y., Shick, A. B., Volobuev, V. V., Springholz, G., Holý, V., Wunderlich, J., Jungwirth, T. & Výborný, K. Magnetic anisotropy in antiferromagnetic hexagonal MnTe. *Phys. Rev. B* **96**, 214418 (2017).

36 Watanabe, R., Yoshimi, R., Shirai, M., Tanigaki, T., Kawamura, M., Tsukazaki, A., Takahashi, K. S., Arita, R., Kawasaki, M. & Tokura, Y. Emergence of interfacial conduction and ferromagnetism in MnTe/InP. *Appl. Phys. Lett.* **113**, 181602 (2018).

37 Chilcote, M., Mazza, A. R., Lu, Q., Gray, I., Tian, Q., Deng, Q., Moseley, D., Chen, A. H., Lapano, J., Gardner, J. S., Eres, G., Ward, T. Z., Feng, E., Cao, H., Lauter, V., McGuire, M. A., Hermann, R., Parker, D., Han, M. G., Kayani, A., Rimal, G., Wu, L., Charlton, T. R., Moore, R. G. & Brahlek, M. Stoichiometry-Induced Ferromagnetism in Altermagnetic Candidate MnTe. *Adv. Funct. Mater.* **34**, 202405829 (2024).

38 He, Q. L., Yin, G., Grutter, A. J., Pan, L., Che, X., Yu, G., Gilbert, D. A., Disseler, S. M., Liu, Y., Shafer, P., Zhang, B., Wu, Y., Kirby, B. J., Arenholz, E., Lake, R. K., Han, X. & Wang, K. L. Exchange-biasing topological charges by antiferromagnetism. *Nat. Commun.* **9**, 2767 (2018).

39 Bey, S., Fields, S. S., Combs, N. G., Márkus, B. G., Beke, D., Wang, J., Ievlev, A. V., Zhukovskyi, M., Orlova, T., Forró, L., Bennett, S. P., Liu, X. & Assaf, B. A. Unexpected tuning of the anomalous Hall effect in altermagnetic MnTe thin films. *arXiv:2409.04567* (2024).

40 Kluczyk, K. P., Gas, K., Grzybowski, M. J., Skupiński, P., Borysiewicz, M. A., Fąs, T., Suffczyński, J., Domagala, J. Z., Grasza, K., Mycielski, A., Baj, M., Ahn, K. H., Výborný, K., Sawicki, M. & Gryglas-Borysiewicz, M. Coexistence of anomalous Hall effect and weak magnetization in a nominally collinear antiferromagnet MnTe. *Phys. Rev. B* **110**, 155201 (2024).

41 Liu, Z., Xu, S., DeStefano, J. M., Rosenberg, E., Zhang, T., Li, J., Stone, M. B., Ye, F., Cong, R. & Pan, S. Strain-tunable anomalous Hall effect in hexagonal MnTe. *arXiv:2509.19582* (2025).

42 Smolenski, S., Mao, N., Zhang, D., Guo, Y., Shawon, A., Xu, M., Downey, E., Musall, T., Yi, M. & Xie, W. Strain-tunability of the multipolar Berry curvature in altermagnet MnTe. *arXiv:2509.21481* (2025).

43 Wasscher, J. D. Evidence of weak ferromagnetism in MnTe from galvanomagnetic measurements. *Solid State Commun.* **3**, 169 (1965).

44 Kondo, J. Resistance Minimum in Dilute Magnetic Alloys. *Prog. Theor. Phys.* **32**, 37 (1964).

45 Hien-Hoang, V., Chung, N.-K. & Kim, H.-J. Electrical transport properties and Kondo effect in $\text{La}_{1-x}\text{Pr}_x\text{NiO}_3-\delta$ thin films. *Sci. Rep.* **11**, 5391 (2021).

46 Brinkman, A., Huijben, M., van Zalk, M., Huijben, J., Zeitler, U., Maan, J. C., van der Wiel, W. G., Rijnders, G., Blank, D. H. A. & Hilgenkamp, H. Magnetic effects at the interface between non-magnetic oxides. *Nat. Mater.* **6**, 493 (2007).

47 Chen, G. & Giordano, N. Thickness dependence of the Kondo effect in AuFe films. *Phys. Rev. Lett.* **66**, 209 (1991).

48 Wang, F., Wang, X., Zhao, Y.-F., Xiao, D., Zhou, L.-J., Liu, W., Zhang, Z., Zhao, W., Chan, M. H. W., Samarth, N., Liu, C., Zhang, H. & Chang, C.-Z. Interface-induced sign reversal of the anomalous Hall effect in magnetic topological insulator heterostructures. *Nat. Commun.* **12**, 79 (2021).

49 Groenendijk, D. J., Autieri, C., van Thiel, T. C., Brzezicki, W., Hortensius, J., Afanasiev, D., Gauquelin, N., Barone, P., Van Den Bos, K. & van Aert, S. Berry phase engineering at oxide interfaces. *Phys. Rev. Res.* **2**, 023404 (2020).

50 Fijalkowski, K. M., Hartl, M., Winnerlein, M., Mandal, P., Schreyeck, S., Brunner, K., Gould, C. & Molenkamp, L. W. Coexistence of surface and bulk ferromagnetism mimics skyrmion Hall effect in a topological insulator. *Phys. Rev. X* **10**, 011012 (2020).

51 Yang, L., Wysocki, L., Schöpf, J., Jin, L., Kovács, A., Gunkel, F., Dittmann, R., van Loosdrecht, P. H. M. & Lindfors-Vrejoiu, I. Origin of the hump anomalies in the Hall resistance loops of ultrathin $\text{SrRuO}_3/\text{SrIrO}_3$ multilayers. *Phys. Rev. Mater.* **5**, 014403 (2021).

52 Kimbell, G., Sass, P. M., Woltjes, B., Ko, E. K., Noh, T. W., Wu, W. & Robinson, J. W. A. Two-channel anomalous Hall effect in SrRuO_3 . *Phys. Rev. Mater.* **4**, 054414 (2020).

53 Onoda, S., Sugimoto, N. & Nagaosa, N. Intrinsic Versus Extrinsic Anomalous Hall Effect in Ferromagnets. *Phys. Rev. Lett.* **97**, 126602 (2006).

54 Kresse, G. & Joubert, D. From ultrasoft pseudopotentials to the projector augmented-wave method. *Phys. Rev. B* **59**, 1758 (1999).

55 Perdew, J. P., Burke, K. & Ernzerhof, M. Generalized Gradient Approximation Made Simple. *Phys. Rev. Lett.* **77**, 3865 (1996).

56 Dudarev, S. L., Botton, G. A., Savrasov, S. Y., Humphreys, C. J. & Sutton, A. P. Electron-energy-loss spectra and the structural stability of nickel oxide: An LSDA+U study. *Phys. Rev. B* **57**, 1505 (1998).

57 Souza, I., Marzari, N. & Vanderbilt, D. Maximally localized Wannier functions for entangled energy bands. *Phys. Rev. B* **65**, 035109 (2001).

58 Varnava, N. & Vanderbilt, D. Surfaces of axion insulators. *Phys. Rev. B* **98**, 245117 (2018).

59 Chapon, L. C., Manuel, P., Radaelli, P. G., Benson, C., Perrott, L., Ansell, S., Rhodes, N. J., Raspino, D., Duxbury, D., Spill, E. & Norris, J. Wish: The New Powder and Single Crystal Magnetic Diffractometer on the Second Target Station. *Neutron News* **22**, 22 (2011).

60 Arnold, O., Bilheux, J. C., Borreguero, J. M., Buts, A., Campbell, S. I., Chapon, L., Doucet, M., Draper, N., Ferraz Leal, R., Gigg, M. A., Lynch, V. E., Markvardsen, A., Mikkelsen, D. J., Mikkelsen, R. L., Miller, R., Palmen, K., Parker, P., Passos, G., Perring, T. G., Peterson, P. F., Ren, S., Reuter, M. A., Savici, A. T., Taylor, J. W., Taylor, R. J., Tolchenov, R., Zhou, W. & Zikovsky, J. Mantid—Data analysis and visualization package for neutron scattering and μ SR experiments. *Nucl. Instrum. Methods Phys. Res., Sect. A* **764**, 156 (2014).

61 Zhou, L.-J. Data for “Surface-State-Driven Anomalous Hall Effect in Altermagnetic MnTe Films”. *Zenodo* <https://doi.org/10.5281/zenodo.18065282> (2025).